

Graphene transmembrane nanofluidic devices: fabrication strategies and ion transport Kanq, X.

Citation

Kang, X. (2025, November 20). *Graphene transmembrane nanofluidic devices: fabrication strategies and ion transport*. Retrieved from https://hdl.handle.net/1887/4283179

Version: Publisher's Version

Licence agreement concerning inclusion of doctoral

License: thesis in the Institutional Repository of the University

of Leiden

Downloaded from: https://hdl.handle.net/1887/4283179

Note: To cite this publication please use the final published version (if applicable).

Experimental strategies to fabricate mechanically exfoliated graphene sub-nanofluidic devices

Mechanically exfoliated graphene is highly attractive for ion transport devices and transmembrane applications because of its excellent crystallinity and minimal defects. However, the small size and difficulty in manipulating exfoliated graphene represent significant challenges in fabricating large quantities of reliable devices to build statistically robust datasets. This study offers a systematic investigation of the experimental procedures involved in preparing free-standing graphene subnanofluidic devices, identifying potential pitfalls at each fabrication step that may lead to chip damage, graphene delamination, leakage, and partial wetting. Potential solutions are proposed to overcome these challenges associated with the use of mechanically exfoliated graphene in device fabrication, aiming to facilitate the development of high-quality graphene-based devices for transmembrane applications.

Keywords: graphene, ion transport, nanopore, transmembrane electrode, delamination, mechanical exfoliation.

This chapter was published as an article:

Xiaofang Kang, Wangyang Fu, Grégory F. Schneider. Carbon, 2025,120005.

2.1 Introduction.

Graphene, a one-atom-thin material with a π -system and exceptional mechanical strength, has opened up many opportunities for various applications¹⁻³. One promising application is its use as a barrier membrane for gas or ion separation. Research has demonstrated that graphene is impermeable to gases as small as He⁴, so pristine graphene cannot achieve gas molecule sieving unless defects are introduced. In 2014, a study experimentally revealed that the smallest particle, a proton, can pass through a perfect single-layer graphene⁵, opening up the possibility of using pristine graphene for proton separation. Recent studies have clarified that proton permeation primarily arises from nanoripples and wrinkles on the graphene surface, which stretch lattice strain in the graphene and reduce the barrier energy for protons⁶. However, the graphene used in this experiment was supported by a Nafion film rather than being fully suspended. The presence of Nafion may introduce doping effects or alter the hydrophobicity of the graphene surface, potentially influencing the mechanism of proton permeation. To fully understand this mechanism through pristine graphene, it is necessary to eliminate the influence of the Nafion support.

However, using free-standing graphene in sub-nanofluidic devices still faces challenges^{7,8}, such as the difficulty and time-consuming process of transferring micrometer-scale, perfectly mechanically exfoliated graphene flakes^{9,10} over the target area. These low fabrication success rates hinder large-scale production, limit statistically significant data acquisition, and therefore impair the device success rate, preventing further study of ion transport phenomena.

To address these challenges and understand the factors hindering the practical application of graphene in sub-nanofluidic devices, this chapter describes a systematic investigation of the entire experimental workflow – from device preparation to final measurement. The analysis pinpointed three critical factors behind the low device yield: (1) mechanical strain induced on the suspended graphene membrane during chip assembly (52.4%), often resulting in complete delamination or damage. (2) Inadequate wetting and contamination issues (24.2%), and (3) partial delamination of the graphene membrane (18.4%). These factors collectively account for 95% of device issues, highlighting their significance in the fabrication process and the need for targeted solutions to improve overall yield. Strategies are proposed to increase the success rate: (1) redesigning the flow cell with softer O-rings and enlarged central apertures to decrease the mechanical stress induced to the graphene membrane, (2) optimizing the hydrophilicity of clean transfer processes and implementing oxygen plasma treatment of the flow cell

microchannels, and (3) integrating a robust adhesion layer to prevent delamination¹¹. Understanding and improving the reliability and reproducibility of these devices would shed light on the ion transport mechanisms and accelerate the development of potential applications such as proton-conducting membranes^{5,6}, water purification^{12,13}, ion sieving¹⁴⁻¹⁷, and osmotic power generation devices^{18,19}.

2.2 Results and Discussion.

The "Scotch tape" technique was used to isolate the single-layer graphene (Figure S1) from graphite on a silicon wafer with a 285 nm-thick layer of silicon dioxide (SiO₂)²⁰. Firstly, an optical microscope identified monolayer graphene based on its optical contrast^{21,22}. Raman spectroscopy was then employed to distinguish between single-layer and multilayer graphene flakes²³, with monolayer graphene identified by a sharp 2D peak (~2700 cm⁻¹), and a 2D peak intensity approximately four times higher than that of the G peak (~1580 cm⁻¹) intensity^{24,25}.

Monolayer exfoliated graphene was transferred onto a silicon nitride (SiN) carrier chip with a one-micrometer-sized hole using the "wedging transfer" technique²⁶. This method involves dropping a CAB polymer solution (30 mg/mL, cellulose acetate butyrate, *i.e.*, CAB in ethyl acetate) onto the monolayer graphene flake area on a Si wafer to act as a protective mask, followed by 10 min of solvent evaporation. The wafer is then treated with oxygen plasma to make its surface hydrophilic. Next, the freshly treated wafer is dipped into the CAB solution and dried for 10 min. The hydrophilic wafer with hydrophobic CAB polymer is submerged in water and wedged off the wafer by sliding it at an angle, causing the CAB film with monolayer graphene to peel off the Si wafer and float on the water surface. Under a microscope, the monolayer graphene is precisely aligned with the target micropore on the SiN chip, which is submerged at the bottom of the water. Gradually removing the water between the graphene and the chip, positions the graphene over the ~1 μm hole. Finally, the CAB film is dissolved using ethyl acetate.

The graphene-on-chip was mounted into a microfluidic flow cell with two chambers, known as the "trans" and "cis". To wet the micro flow channel, inject a 1:1 (vol/vol) mixture of ethanol and ultrapure water into the inlets²⁷, followed by the injection of electrolyte (0.1 M HCl) and the placement of Ag/AgCl electrodes. A voltage was applied across these two electrodes to measure the ion current (see Figure 1a).

The priority was to evaluate whether the assembly process (Figure 1b) could potentially damage the graphene or the suspended SiN membrane (see Figure 1c). Any damage to these membranes could create additional current flow paths, leading to leakage. If the graphene membrane remained intact after mounting the chip on the

flow cell, it was necessary to verify that ions pass only through the suspended graphene region as expected, rather than leaking through the interfacial channel between the graphene and the substrate. Also, over time, if graphene delaminated from the chips, an increase in ion current would be measured due to uncontrolled leakage (Figure 1e).

In addition to different causes of leakage, it is crucial to determine whether the measured conductance originates from the graphene itself or if other factors influenced the results. Also, non-linearities in conductance-voltage plots suggest the absence of an ion path: ions accumulate at the graphene-water interface, intrinsically building up a capacitor. Moreover, very low conductances or non-linearities could be influenced by other factors such as air bubbles trapped in the pore, graphene hydrophobicity, or polymer residues introduced during the graphene transfer process (see Figure 1d).

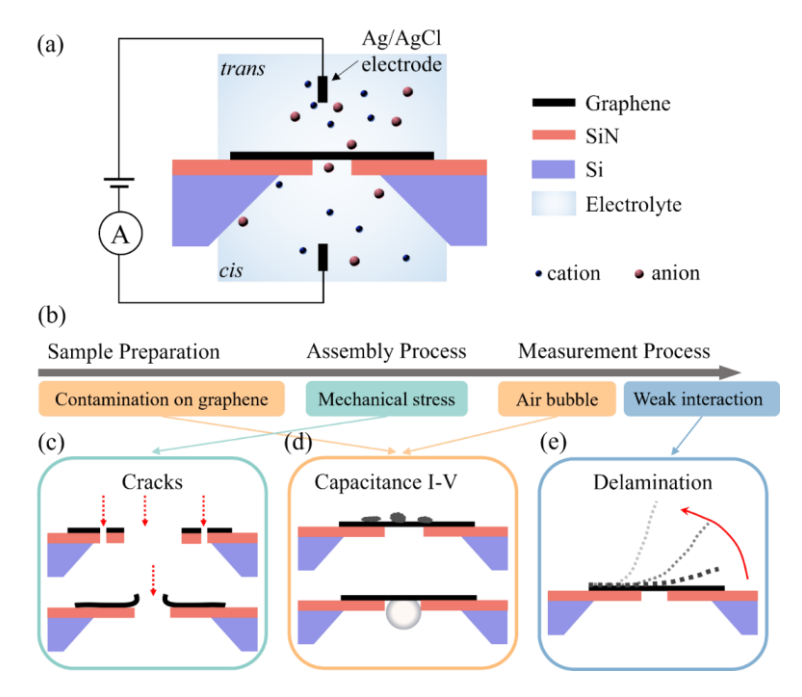


Figure 1. Experimental setup and potential factors causing device unsuccess in mechanically exfoliated graphene sub-nanofluidic devices. (a) Schematic of the measurement set-up, featuring a graphene membrane suspended over a micropore in a SiN chip, mounted in a microfluidic flow cell with cis and trans chambers. Ag/AgCl electrodes are used to apply voltage and measure ion current. (b) An overview analysis of the possible causes leading to unsuccessful devices during the sample preparation, assembly process, and measurement process. (c) Illustration of potential damage to the graphene or SiN membrane

during chip mounting in the flow cell, which can lead to unintended current pathways. (d) Representative *I-V* curves showing capacitive effects, possibly caused by air bubbles due to graphene hydrophobicity or polymer residues from the transfer process. (e) Schematic of graphene delamination over time, resulting in increased leakage currents.

The critical process of mounting the chip in the flow cell was examined first. The custom-designed polymethyl methacrylate (PMMA) flow cell comprises two separate parts, each featuring inlet and outlet ports for fluid flow. During assembly, the graphene-covered chip is carefully sandwiched between these two parts, ensuring that the free-standing graphene areas align precisely with the inlet channels. To prevent liquid leakage, O-rings are securely affixed to both sides of the chip and each part of the flow cell (Figure S2). Following chip installation, introduce 0.1 M HCl electrolyte through the inlet ports and position Ag/AgCl electrodes in the inlet channels of each flow cell component to apply a direct current voltage across the graphene membrane. To avoid the risk of voltage-induced graphene breakdown²⁸, a small voltage range of -100 mV to 100 mV, with 10 mV increments, is used.

A total of 103 devices with mechanically exfoliated graphene were tested. Of these, 54 devices (52.4%) exhibited conductivity equal to or exceeding that of bare chips with 1 µm pores. Conductivity equal to that of 1 µm holes indicates complete graphene removal, while higher conductivity suggests the presence of additional pathways beyond the pore itself. Post-measurement scanning electron microscopy (SEM) analysis revealed varying degrees of SiN membrane damage (Figure 2a): (i) minor cracking of the SiN window with intact free-standing graphene, (ii) extensive SiN membrane damage, with pore area that is supposed to be covered by graphene, but no graphene anymore, and (iii) near-complete destruction of the SiN window.

The severity of this damage is particularly noteworthy given that both SiN and graphene membranes were intact before flow cell mounting. The results of significant leakage currents and extensive damage under SEM after loading implicate the loading process as the primary cause of membrane damage. That could be due to the force during chip installation to ensure a tight seal with the O-rings, which are critical for eliminating gaps between flow cell components and chips.

The nitrile compound O-rings used in the flow cell with high hardness and poor viscoelasticity, resulting in a limited contact area with the chip (Figures 2b and 2c). This limited contact area hindered the O-ring's ability to conform to the chip surface, leading to localized stress concentrations at the membrane interface. During the mounting process, the rigid O-ring material likely exerted excessive mechanical stress on the membrane, potentially inducing cracks or breaks (Figure 2d). Analysis

revealed that the majority of unsuccess can be traced to mechanical stresses induced by measurement setups (flow cells) during the device assembly process. Notably, 49 devices (47.6%) did not show such a high leakage, due to cautious operation during the chip mounting step.

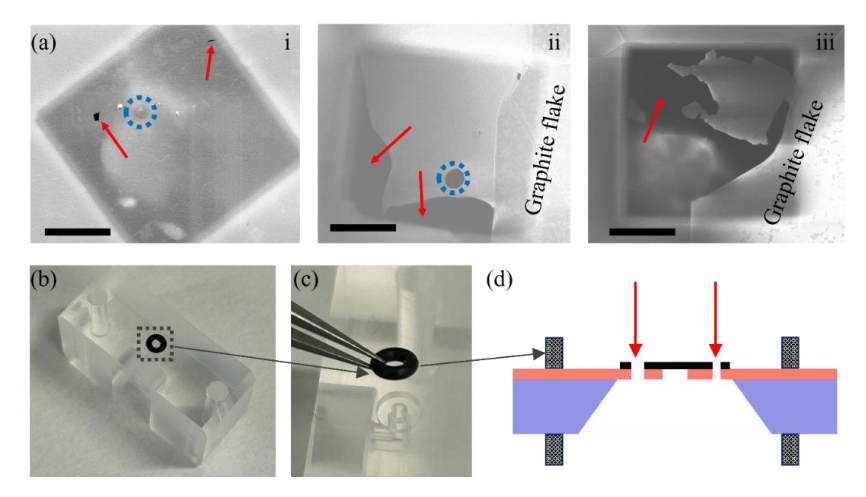


Figure 2. Analysis of the device unsuccess due to strain caused by an inadequate flow cell design. (a) SEM images revealing damage to SiN window after ionic transport: (i) localized crack (red arrow) with intact free-standing graphene (blue dashed circle), (ii) extensive damage to SiN membrane and loss of free-standing graphene, (iii) Near-complete rupture of SiN membrane. Scale bar: 4 μ m. (b, c) Photographs of the custom-designed flow cell, highlighting the O-ring component. (d) Schematic cross-section illustrating chip loading with the O-ring, showing localized pressure distribution and potential crack formation sites.

After excluding devices with high leakage, a subset of samples exhibited extreme *I-V* curve asymmetry, indicative of capacitive rather than resistive characteristics. These samples were categorized into three groups: (1) ultra-low conductance (8 out of the 103 devices, 7.8%): these devices exhibited a mere 10 pA current (Figure 3a), suggesting near-complete blockage within the pore region. This phenomenon is hypothesized to result from the presence of nanobubbles²⁹, either on the graphene surface or the wall of microflow channels, impeding ion transport (Figure 3d). (2) Subtle asymmetry (9 devices, 8.7%): these samples displayed mild asymmetry under an applied voltage of -100 mV (Figure 3b). (3) High-current asymmetry (8 devices, 7.8%): this group exhibited elevated currents coupled with pronounced asymmetry (Figure 3c).

The asymmetry observed in Figures 3b and 3c can be induced by various factors, such as channel geometry and non-uniform surface charge distribution³⁰. However, in these experiments, only a monolayer graphene layer was used as a channel,

eliminating the inherent asymmetry in the channel geometry. Instead, this asymmetry likely stems from non-uniform charge distribution along the graphene channel, likely caused by residual polymer from the transfer process or adsorbed airborne contaminants on the graphene surface (Figure 3e). These factors can induce localized charges, resulting in the observed asymmetric *I-V* curves. In total, 25 devices (24.2% of the 103 devices) exhibited this asymmetric behavior and were consequently excluded from further analysis.

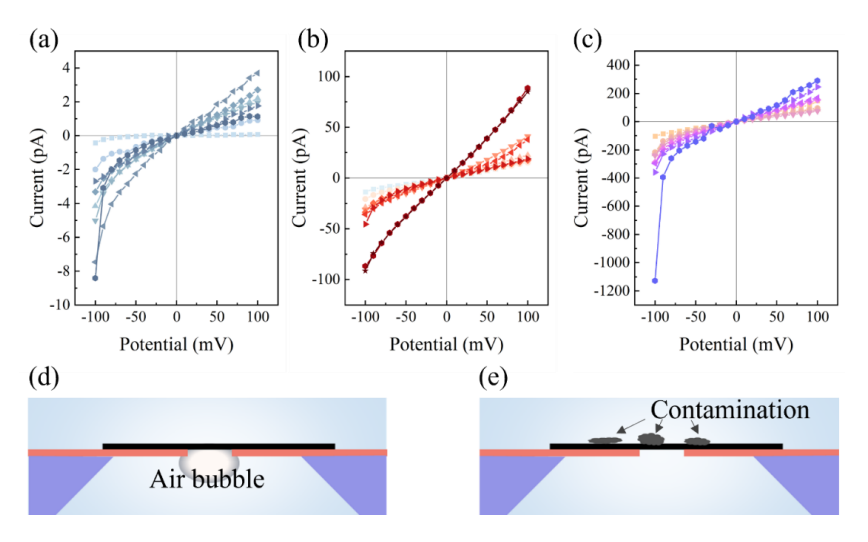


Figure 3. Asymmetry *I-V* **curves and underlying mechanisms.** (a) Ultra-low conductance regime, (b) subtle asymmetry, and (c) obvious asymmetry coupled with large currents. (d) Schematic illustration of nanobubble-induced ion transport obstruction, corresponding to the ultra-low conductance regime in (a). (e) Conceptual model of non-uniform surface charge distribution caused by contaminants, leading to asymmetric *I-V* characteristics observed in (b) and (c).

Analysis of the remaining 24 devices revealed two subsets with different conductances. The first subset, comprising 12 devices (11.7% of the total), exhibited *I-V* curves with currents ranging from 1 nA to 20 nA at 100 mV (Figure 4a). These devices displayed areal conductance values between 1 to 25 S cm⁻², significantly exceeding previously reported proton conductance values for graphene³¹. This anomalously high conductance is attributed to the partial delamination of the graphene membrane from the substrate (Figure 4b), resulting in the formation of additional ionic current pathways.

The second subset, also comprising 12 devices (11.7% of the total), demonstrated linear *I-V* curves and low conductance values when measured in 0.1 M HCl solution.

This linearity precludes graphene surface contamination and charge-induced I-V asymmetry as potential factors. The observed low conductance aligns with values reported in the literature³¹, suggesting minimal contribution from leakage currents and a dominant role of the intrinsic properties of the graphene membrane in determining its conductance (Figure 4d). Four of these 12 devices displayed currents ranging from 100 pA to 250 pA at 100 mV (Figure 4c(i)), corresponding to areal conductances spanning from 0.17 to 0.30 S cm⁻². The remaining eight devices demonstrated lower areal conductances, ranging from 0.01 to 0.1 S cm⁻² (Figure 4c(ii)). The conductivity values for a subset of these devices vary by less than an order of magnitude, indicating consistent and reproducible graphene properties. This final group of 12 devices, representing 11.7% of the total sample, most closely reflects the expected behavior of pristine graphene membranes. The observed conductance in these devices likely includes contributions from nanoripples and wrinkles on the graphene surface, which are unavoidably introduced during the graphene transfer process. These morphologies create localized curvature and strain in the graphene lattice, which were reported to lower the proton energy barrier, facilitate proton adsorption, and create preferential pathways for proton transport⁶.

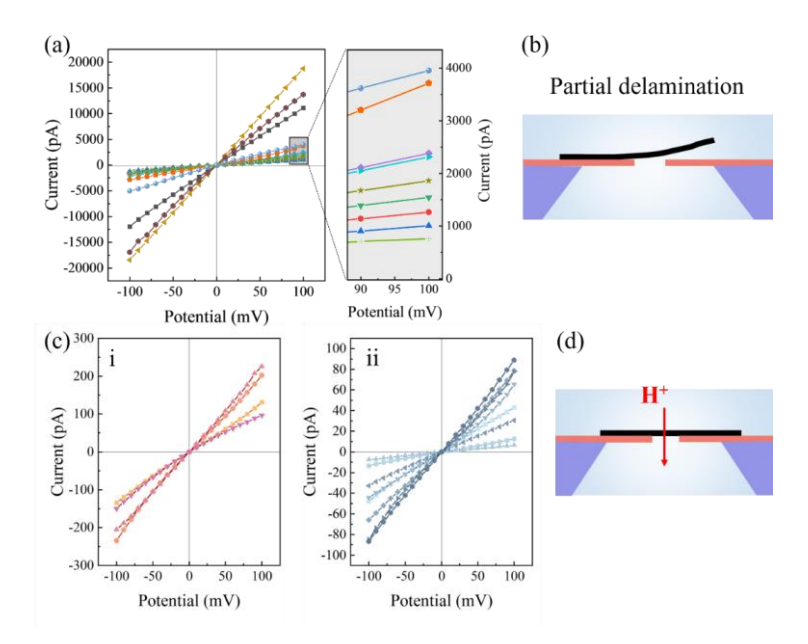


Figure 4. Symmetry *I-V* **curves for partially delaminated devices and successful devices.** (a) *I-V* curves of 12 devices (11.7%) exhibiting partial delamination, with currents ranging from 1 nA to 20 nA at 100 mV. Inset: magnified view of the 90–100 mV range for nine representative devices. (b) Schematic cross-section illustrating partial graphene delamination,

explaining the mechanism for the high conductance observed in (a). (c) *I-V* curves of devices displaying expected graphene behavior: (i) four devices with areal conductances of 0.17, 0.30, 0.26, and 0.19 S cm⁻², and (ii) eight devices exhibiting lower areal conductances ranging from 0.01–0.1 S cm⁻². (d) Conceptual model of selective proton transport through an intact graphene membrane in a nanofluidic device.

To further study the long-term stability of the 12 successful devices, the graphene transconductance was tested in various electrolyte solutions (0.1 M of HCl, KCl, CuCl₂, CaCl₂, FeCl₃) by repeatedly exchanging the electrolyte. Seven devices showed increased conductance, eventually matching that of the chip itself (Figure 5a) after multiple exchange cycles. From the images captured before performing *I-V* measurements, monolayer graphene can be seen over the 1 μm pore area, with surrounding graphite flakes serving as a reference (it can also be seen from Figure 2a(ii) and (iii)). However, after ion transport measurement, the graphene flake was gone from the chip (Figure 5c). This delamination can be attributed to the small size of the mechanically exfoliated graphene flakes (~10 μm diameter). Although monolayer graphene initially covered the hole, the exposed edges and hydrophilicity of the silicon nitride surface increase the probability for water to intercalate from the edge area of the graphene flake to between the flake and the substrate, leading to gradual delamination (Figure 5b).

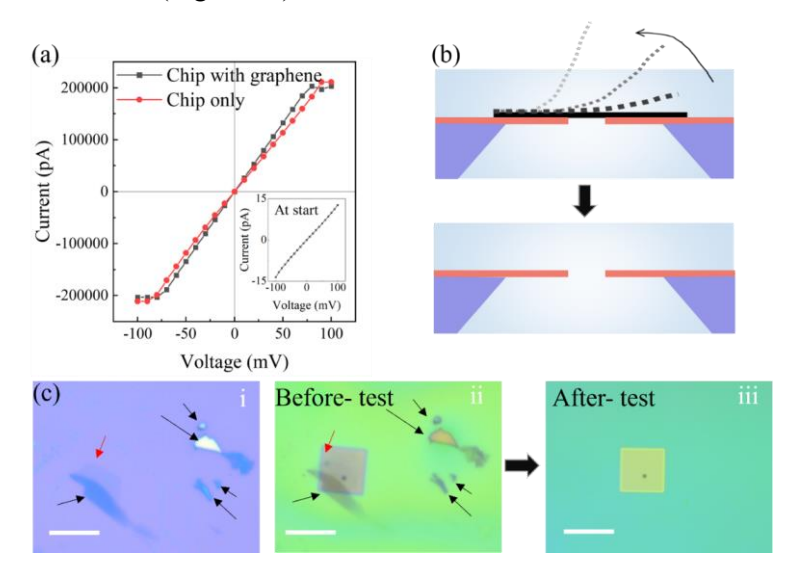


Figure 5. Time-dependent delamination of graphene in nanofluidic devices (a) *I-V* curves of seven devices (out of 12) exhibiting time-lapse graphene delamination. (b) Schematic of the gradual graphene delamination process. (c) Optical image: (i) mechanically exfoliated monolayer graphene (red arrow) and reference graphite flake (black arrow) on a silicon wafer.

(ii) Chip with transferred graphene before testing. (iii) Post-test chip surface, showing the absence of both graphene and reference flakes, indicating complete delamination. Scale bar: 20 μm.

These findings, based on statistical analyses of the 103 device situations (as summarized in Table S1), highlight the need to reduce mechanical strain, reduce contamination, increase wetting, and avoid delamination through innovative design solutions and optimized fabrication protocols. Several approaches are proposed to tackle these challenges. Firstly, to mitigate stress-induced graphene damage during the chip mounting, optimizing the flow cell design is essential. Specifically, fabricating sample chambers with dimensions precisely tailored to the chip specifications, ensuring appropriate chamber height to minimize the loading process (Figure S3). Additionally, incorporating softer O-rings with larger contact areas can evenly distribute stress evenly across the chip surface. Furthermore, increasing the central aperture size of the O-rings allows their position further from the suspended membrane, reducing localized stress on this fragile membrane. Secondly, to minimize contaminant residues, implementing refined graphene transfer protocols is recommended. For example, using cleaner polymers, such as the paraffin-assisted transfer method reported by Kong et al. 32. Additionally, by optimizing the removal of residue, for example, by controlled heating during the polymer removal step or post-transfer annealing, has further contributed to reducing contamination. Thirdly, to address improper wetting, two approaches are suggested: (1) treat the flow cell microchannels with oxygen plasma before chip loading, rendering channel surfaces hydrophilic, and (2) improve the wetting by using a 1:1 ethanol-water solution. Increasing the number of rinsing cycles and extending soaking time with this solution could enhance the chip wetting, ensuring also better contact between the electrolyte and the graphene. Lastly, to prevent the gradual delamination of graphene, enhancing the adhesion energy between the membrane and substrate is important. We propose to pre-coating chips with hydrophobic self-assembled monolayers such as hexamethyldisilazane or octadecyltrichlorosilane. These coatings create an interfacial increasing the interaction between the graphene and the substrate.

2.3 Conclusions.

This chapter systematically investigated the fabrication process of mechanically exfoliated graphene sub-nanofluidic devices through a comprehensive statistical analysis. The examination revealed that devices break at different stages: 52.4% of devices were damaged during the mounting of the chip due to mechanical stress, 16.5% were affected by contaminant residues during graphene transfer, 7.8% exhibited poor wetting, and 11.7% showed large leakage currents at the graphene-

substrate interface. Notably, only 11.6% of devices demonstrated intrinsic graphene transmembrane properties, with proton conductance ranging from 0.01 to 0.3 S cm². However, 58.3% of these experienced gradual delamination, resulting in a mere 4.9% of devices remaining stable throughout testing.

These findings provide crucial insights into the challenges impeding successful device fabrication and guiding targeted solutions. Proposed approaches to address these issues, include: (1) optimized flow cell designs to mitigate mechanical stress, (2) cleaner transfer protocols to minimize contamination, (3) enhanced wetting/sealing strategies, and (4) surface modifications to prevent delamination. This comprehensive understanding enables the fabrication of less-delaminating mechanically exfoliated graphene sub-nanofluidic systems, deepening insights into ion transport mechanisms, particularly proton, and facilitating their integration into applications like proton-conducting membranes, ionic/molecular sieving, biosensing, and energy harvesting.

2.4 References.

- [1]. K. S. Novoselov, A. K. Geim, S. V. Morozov, D. Jiang, Y. Zhang, S. V. Dubonos, I. V. Grigorieva and A. A. Firsov. Electric field effect in atomically thin carbon films. *Science* 2004, **306**, 666-669.
- [2]. A. K. Geim and K. S. Novoselov. The rise of graphene. *Nat Mater* 2007, **6**, 183-191.
- [3]. A. H. Castro Neto, F. Guinea, N. M. R. Peres, K. S. Novoselov and A. K. Geim. The electronic properties of graphene. *Rev Mod Phys* 2009, **81**, 109-162.
- [4]. J. S. Bunch, S. S. Verbridge, J. S. Alden, A. M. van der Zande, J. M. Parpia, H. G. Craighead and P. L. McEuen. Impermeable atomic membranes from graphene sheets. *Nano Lett* 2008, **8**, 2458-2462.
- [5]. S. Hu, M. Lozada-Hidalgo, F. C. Wang, A. Mishchenko, F. Schedin, R. R. Nair, E. W. Hill, D. W. Boukhvalov, M. I. Katsnelson, R. A. Dryfe, I. V. Grigorieva, H. A. Wu and A. K. Geim. Proton transport through one-atom-thick crystals. *Nature* 2014, 516, 227-230.
- [6]. O. J. Wahab, E. Daviddi, B. Xin, P. Z. Sun, E. Griffin, A. W. Colburn, D. Barry, M. Yagmurcukardes, F. M. Peeters, A. K. Geim, M. Lozada-Hidalgo and P. R. Unwin. Proton transport through nanoscale corrugations in two-dimensional crystals. *Nature* 2023, 620, 782-786.
- [7]. G. F. Schneider, S. W. Kowalczyk, V. E. Calado, G. Pandraud, H. W. Zandbergen, L. M. Vandersypen and C. Dekker. DNA translocation through graphene nanopores. *Nano Lett* 2010, **10**, 3163-3167.
- [8]. C. A. Merchant, K. Healy, M. Wanunu, V. Ray, N. Peterman, J. Bartel, M. D. Fischbein, K. Venta, Z. Luo, A. T. Johnson and M. Drndic. DNA translocation through graphene nanopores. *Nano Lett* 2010, **10**, 2915-2921.
- [9]. M. Lozada-Hidalgo, S. Zhang, S. Hu, V. G. Kravets, F. J. Rodriguez, A. Berdyugin, A. Grigorenko and A. K. Geim. Giant photoeffect in proton transport through graphene membranes. *Nat Nanotechnol* 2018, 13, 300-303.
- [10]. E. Griffin, L. Mogg, G. P. Hao, G. Kalon, C. Bacaksiz, G. Lopez-Polin, T. Y.

- Zhou, V. Guarochico, J. Cai, C. Neumann, A. Winter, M. Mohn, J. H. Lee, J. Lin, U. Kaiser, I. V. Grigorieva, K. Suenaga, B. Ozyilmaz, H. M. Cheng, W. Ren, A. Turchanin, F. M. Peeters, A. K. Geim and M. Lozada-Hidalgo. Proton and Li-ion permeation through graphene with eight-atom-ring defects. *ACS Nano* 2020, **14**, 7280-7286.
- [11]. B. S. Can, N. V. V. Bluemel, E. P. van Geest, M. Makurat, J. M. van Ruitenbeek and G. F. Schneider. A perspective on graphene junctions for recognition tunneling. *Appl Phys Lett* 2024, **124**, 210501.
- [12]. M. Heiranian, A. B. Farimani and N. R. Aluru. Water desalination with a single-layer MoS₂ nanopore. *Nat Commun* 2015, **6**, 8616.
- [13]. S. P. Surwade, S. N. Smirnov, I. V. Vlassiouk, R. R. Unocic, G. M. Veith, S. Dai and S. M. Mahurin. Water desalination using nanoporous single-layer graphene. *Nat Nanotechnol* 2015, **10**, 459-464.
- [14]. J. Abraham, K. S. Vasu, C. D. Williams, K. Gopinadhan, Y. Su, C. T. Cherian, J. Dix, E. Prestat, S. J. Haigh, I. V. Grigorieva, P. Carbone, A. K. Geim and R. R. Nair. Tunable sieving of ions using graphene oxide membranes. *Nat Nanotechnol* 2017, 12, 546-550.
- [15]. Y. Qian, J. Shang, D. Liu, G. Yang, X. Wang, C. Chen, L. Kou and W. Lei. Enhanced ion sieving of graphene oxide membranes via surface amine functionalization. *J Am Chem Soc* 2021, **143**, 5080-5090.
- [16]. L. Guo, Y. Liu, H. Zeng, S. Zhang, R. Song, J. Yang, X. Han, Y. Wang and L. Wang. Covalently functionalized nanopores for highly selective separation of monovalent ions. *Adv Mater* 2024, **36**, e2307242.
- [17]. S. Yasuda, H. Matsushima, K. Harada, R. Tanii, T. O. Terasawa, M. Yano, H. Asaoka, J. S. Gueriba, W. A. Dino and K. Fukutani. Efficient hydrogen isotope separation by tunneling effect using graphene-based heterogeneous electrocatalysts in electrochemical hydrogen isotope pumping. *ACS Nano* 2022, **16**, 14362-14369.
- [18]. X. Liu, M. He, D. Calvani, H. Qi, K. Gupta, H. J. M. de Groot, G. J. A. Sevink, F. Buda, U. Kaiser and G. F. Schneider. Power generation by reverse electrodialysis in a single-layer nanoporous membrane made from core-rim polycyclic aromatic hydrocarbons. *Nat Nanotechnol* 2020, **15**, 307-312.

- [19]. J. Safaei and G. X. Wang. Progress and prospects of two-dimensional materials for membrane-based osmotic power generation. *Nano Res Energy* 2022, **1**, 9120008.
- [20]. K. S. Novoselov, D. Jiang, F. Schedin, T. J. Booth, V. V. Khotkevich, S. V. Morozov and A. K. Geim. Two-dimensional atomic crystals. *Proc Natl Acad Sci U S A* 2005, **102**, 10451-10453.
- [21]. P. Blake, E. W. Hill, A. H. Castro Neto, K. S. Novoselov, D. Jiang, R. Yang, T. J. Booth and A. K. Geim. Making graphene visible. *Appl Phys Lett* 2007, **91**, 063124.
- [22]. Z. H. Ni, H. M. Wang, J. Kasim, H. M. Fan, T. Yu, Y. H. Wu, Y. P. Feng and Z. X. Shen. Graphene thickness determination using reflection and contrast spectroscopy. *Nano Lett* 2007, 7, 2758-2763.
- [23]. L. M. Malard, M. A. Pimenta, G. Dresselhaus and M. S. Dresselhaus. Raman spectroscopy in graphene. *Phys Rep* 2009, **473**, 51-87.
- [24]. A. C. Ferrari, J. C. Meyer, V. Scardaci, C. Casiraghi, M. Lazzeri, F. Mauri, S. Piscanec, D. Jiang, K. S. Novoselov, S. Roth and A. K. Geim. Raman spectrum of graphene and graphene layers. *Phys Rev Lett* 2006, 97, 187401.
- [25]. D. Graf, F. Molitor, K. Ensslin, C. Stampfer, A. Jungen, C. Hierold and L. Wirtz. Spatially resolved Raman spectroscopy of single- and few-layer graphene. *Nano Lett* 2007, 7, 238-242.
- [26]. G. F. Schneider, V. E. Calado, H. Zandbergen, L. M. Vandersypen and C. Dekker. Wedging transfer of nanostructures. *Nano Lett* 2010, **10**, 1912-1916.
- [27]. M. Graf, M. Lihter, M. Thakur, V. Georgiou, J. Topolancik, B. R. Ilic, K. Liu, J. Feng, Y. Astier and A. Radenovic. Fabrication and practical applications of molybdenum disulfide nanopores. *Nat Protoc* 2019, **14**, 1130-1168.
- [28]. J. Loessberg-Zahl, D. S. de Bruijn, W. T. E. van den Beld, E. Dollekamp, E. Grady, A. Keerthi, J. Bomer, B. Radha, H. J. W. Zandvliet, A. A. Bol, A. van den Berg and J. C. T. Eijkel. Exploring voltage mediated delamination of suspended 2D materials as a cause of commonly observed breakdown. J Phys Chem C 2019, 124, 430-435.

- [29]. E. Beamish, H. Kwok, V. Tabard-Cossa and M. Godin. Precise control of the size and noise of solid-state nanopores using high electric fields. *Nanotechnology* 2012, **23**, 405301.
- [30]. L. J. Cheng and L. J. Guo. Nanofluidic diodes. *Chem Soc Rev* 2010, **39**, 923-938.
- [31]. S. Garaj, W. Hubbard, A. Reina, J. Kong, D. Branton and J. A. Golovchenko. Graphene as a subnanometre trans-electrode membrane. *Nature* 2010, **467**, 190-193.
- [32]. W. S. Leong, H. Wang, J. Yeo, F. J. Martin-Martinez, A. Zubair, P. C. Shen, Y. Mao, T. Palacios, M. J. Buehler, J. Y. Hong and J. Kong. Paraffin-enabled graphene transfer. *Nat Commun* 2019, **10**, 867.

2.5 Appendix.

2.5.1 Materials and Methods.

Natural graphite used for exfoliated graphene was obtained commercially from NGS Naturgraphit. All chemicals were purchased from Sigma-Aldrich and were used as received without further purification.

Oxygen plasma was generated using a capacitively coupled plasma system (Femto, Diener Electronic) at 40 kHz and 200 W at room temperature. To render the surface hydrophilic, a 200 W oxygen plasma treatment was applied for 10 s. Optical images were obtained with a Leica DM 2700M Brightfield microscope containing a Leica MC 120 HD camera. Raman spectra were acquired using a WITEC alpha500 R Confocal Raman Imaging system with a 532 nm, 2 mW laser. Scanning electron microscopy (SEM) was performed using a JEOL SEM 6400 to assess graphene coverage and identify damaged areas in devices that were leaking. SEM imaging was done under a high vacuum with a 10 kV accelerating voltage, 0.1 nA current, and ~10 mm working distance to the lense. Ionic transport measurements were conducted with an Axopatch 200B amplifier and a Digitizer 1550 (Molecular Devices), referenced to a saturated Ag/AgCl electrode, at room temperature within a Faraday cage on a vibration isolation table to minimize noise.

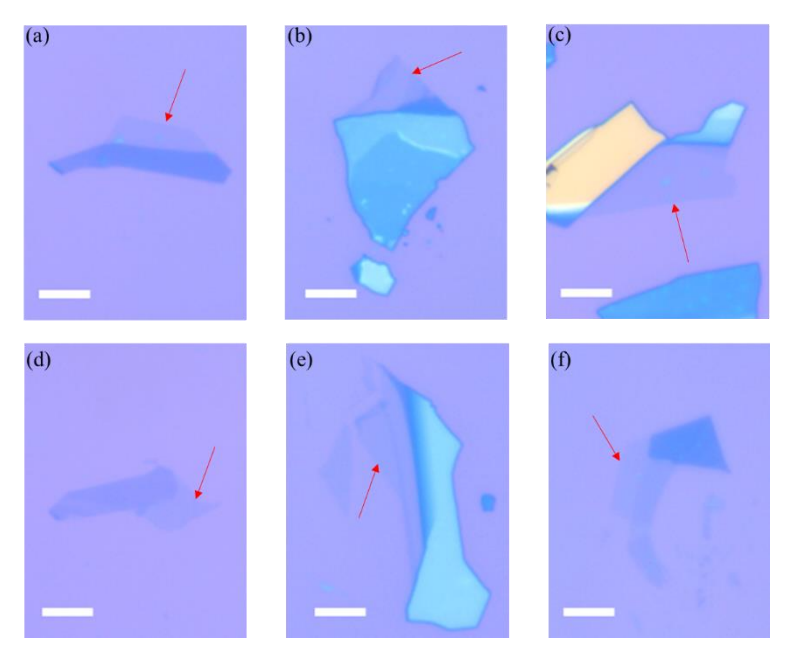


Figure S1. Optical images of mechanically exfoliated monolayer graphene areas, the red arrow indicates the monolayer graphene. Scale bar: 10 μm.

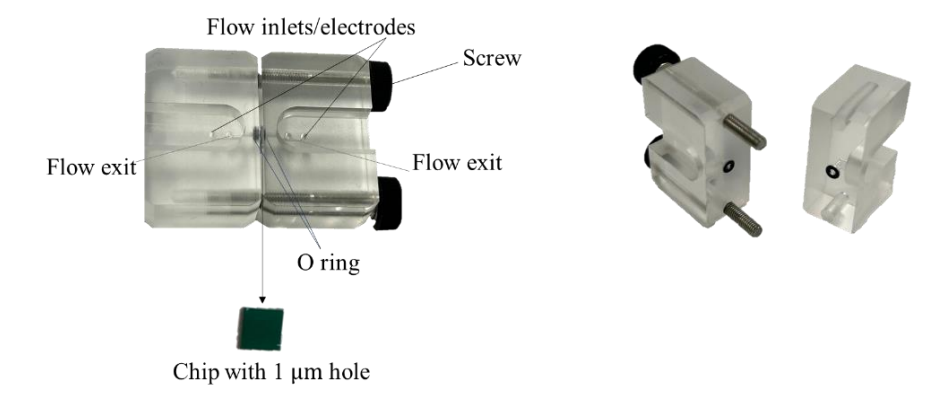


Figure S2. Optical micrograph of a home-made flow cell: different components are marked on the images.

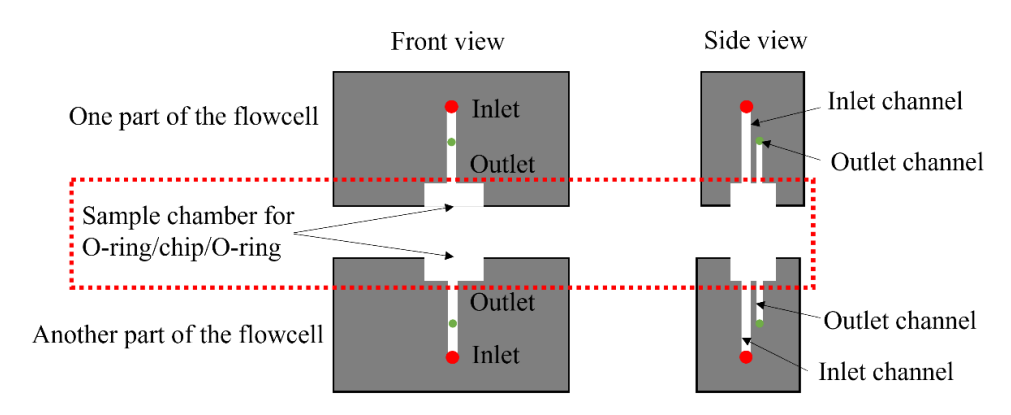


Figure S3. Illustration of the improved flow-cell design, featuring a sample chamber with dimensions precisely tailored to the chip specifications.

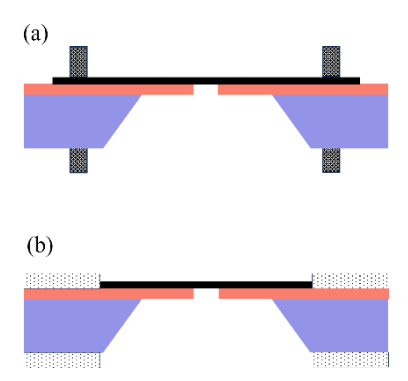


Figure S4. Illustration of the O-ring design improvements. (a) The current O-ring design features a small contact area with graphene. (b) The proposed O-ring design has an enlarged contact area.

Туре	Count	Percentage
Membrane damage (Graphene or SiNx)	54	52.4%
Contaminant residues	17	16.5%
Improper wetting	8	7.7%
Leakage	12	11.7%
Gradual delamination	7	6.8%
Long-term success	5	4.9%
Total	103	100%

Table 1. Statistical analysis of mechanically exfoliated graphene sub-nanofluidic devices (n = 103).